J Mater Sci (2008) 43:748–758
DOI 10.1007/s10853-007-2192-7

Microstructural evolution and mechanical property in dual two-phase intermetallic alloys composed of geometrically close-packed Ni_3X (X: Al and V) containing Nb

Yasuyuki Kaneno · Wataru Soga · Hiroshi Tsuda · Takayuki Takasugi

Received: 17 July 2007 / Accepted: 25 September 2007 / Published online: 31 October 2007

Abstract Dual two-phase intermetallic alloys composed of geometrically close-packed (GCP) structures of Ni_3Al ($L1_2$) and Ni_3V ($D0_{22}$) containing Nb were investigated in terms of microstructural evolution during low-temperature annealing (aging) and the related mechanical properties. The eutectoid region, i.e. the prior Al phase (Ni solid solution) is composed of the lamellar-like structure consisting of Ni_3Al ($L1_2$) and Ni_3V ($D0_{22}$) even at an early aging stage, and then coarsen with increasing aging time. The lamellar-like structure tend to align along $\langle 001 \rangle$ direction and on $\{001\}$ plane in the prior A1 phase (or the $L1_2$ phase). In a wide range of temperature, the dual two-phase intermetallic alloys showed high yield and tensile strength, and also reasonable tensile ductility, accompanied with ductile fracture mode. The observed mechanical properties were less sensitive to the microstructural evolution during low-temperature annealing (aging), meaning that the present dual two-phase intermetallic alloy is promising for a new type of high-temperature structural material.

Introduction

It is well known that attractive high-temperature mechanical properties of Ni-based superalloys arise from their coherent interface structure and fine microstructure composed of a two-phase microstructure consisting of A1 phase (γ:Ni solid solution) and $L1_2$ phase (γ':Ni_3Al). Taking such an excellent microstructure into consideration, a new concept for developing high-temperature structural materials was recently suggested by the present authors. A1 phase (γ:Ni solid solution) was altered with geometrically close packed (GCP) Ni_3X intermetallic phases that are similar to Ni_3Al, and generally exhibit high-phase and microstructural stabilities up to their melting points, because of low-atomic diffusivity owing to their close packed structures [1–3]. Highly coherent interface structure and fine microstructure were expected in such new materials, because GCP Ni_3X intermetallic phases are crystallographically similar each other. Actually, several multi-phase intermetallic alloys composed of, e.g., GCP Ni_3X (X: Al, Ti and Nb) [4, 5], (X: Si, Ti and Nb) [6–8], (X: Al, Ti and V) [9–13] and (X: Al, Nb and V) [14, 15] intermetallic phases have been evaluated, and shown to exhibit stable microstructures at high temperatures.

From such a new concept, 'dual' two-phase intermetallic alloys composed of GCP Ni_3Al ($L1_2$) and Ni_3V ($D0_{22}$) phases containing Ti [9–13] and Nb [14, 15] have been developed, based on Ni_3Al–Ni_3Ti–Ni_3V and Ni_3Al–Ni_3Nb–Ni_3V pseudo-ternary alloy systems, respectively. The dual two-phase intermetallic alloys are composed of Ni_3Al ($L1_2$) and Ni solid solution (A1) phases at high temperature, and Ni solid solution (A1) phase is decomposed into Ni_3Al ($L1_2$) + Ni_3V ($D0_{22}$) by a eutectoid reaction at low-temperature aging. It was shown that the dual two-phase intermetallic alloys exhibit coherent microstructures not only at the micron scale, but also at the sub-micron scale [9, 10, 12, 14, 15]. In addition, the high-temperature mechanical properties, e.g., creep properties of the dual two-phase intermetallic alloys were found to be

Y. Kaneno · W. Soga · H. Tsuda · T. Takasugi
Department of Materials Science, Graduate School of Engineering, Osaka Prefecture University, 1-1 Gakuen-cho, Naka-ku, Sakai, Osaka 599-8531, Japan

T. Takasugi (✉)
Osaka Center for Industrial Materials Research, Institute for Materials Research, Tohoku University, 1-1 Gakuen-cho, Naka-ku, Sakai, Osaka 599-8531, Japan
e-mail: takasugi@mtr.osakafu-u.ac.jp

superior to those of most conventional Ni-based superalloys [11, 13, 15].

In the present study, dual two-phase intermetallic alloys composed of Ni_3Al ($L1_2$) and Ni_3V ($D0_{22}$) phases containing Nb were studied, focusing on microstructural evolution and stability in the *lower* two-phase region (i.e., eutectoid region) during low-temperature aging. Also, the high-temperature mechanical properties, such as yield strength, tensile strength, tensile elongation, and fracture mode were investigated in association with microstructural change during low temperature aging. It is expected that the replacement of Ti by Nb results in improvement of high-temperature mechanical properties of the dual two-phase intermetallic alloys composed of $L1_2$ Ni_3(Al,V,Nb) and $D0_{22}$ Ni_3(V,Al,Nb).

Experimental procedures

Alloy compositions prepared in this study are basically the same, as those used in the previous study [15], and shown in Table 1, Figs. 1 and 2. Alloy No. 15 contains 3at.%Nb while others contain 2.5at.%Nb. It is noted that alloys No. 15 + B and No. 22 + B contain 500wt.ppm boron. Boron-doped alloys were used to evaluate high-temperature tensile properties. Also, specimen preparation is almost the same, as that used in the previous study [15], and, therefore, omitted from this article.

Microstructural observation of dual two-phase intermetallic alloys was carried out by optical microscopy (OM), scanning electron microscopy (SEM), and transmission electron microscopy (TEM). TEM foils cut from the specimens with dual two-phase microstructure were mechanically thinned to about 0.1 mm and finally jet-polished in a mixed solution of 15 mL H_2SO_4 + 85 mL CH_3OH at about 240 K. TEM observation was carried out using a JEM-2000FX operating at 200 kV. The microstructures were in detail analyzed by taking electron diffraction patterns, and bright field (BF) and dark field (DF) images. The diameter of aperture of the objective lens used was small enough to resolve the lower two-phase microstructure, i.e. the eutectoid region. The electron beam direction parallel to one of the $\langle 001 \rangle_{L12}$ directions was used.

Table 1 Chemical compositions and microstructures of alloys used in this study

Alloys	Alloy compositions				
	Ni (at.%)	Al (at.%)	Nb (at.%)	V (at.%)	B (ppm)
15	75	8.75	3	13.25	
15 + B	75	8.75	3	13.25	500
21	75	5	2.5	17.5	
22	75	7.5	2.5	15	
22 + B	75	7.5	2.5	15	500
23	75	10	2.5	12.5	

Vickers hardness was measured in the condition of a load of 300gf and a duration time of 20 s. For tensile test, specimens with a gauge dimension of $2 \times 1 \times 10$ mm^3 were cut by a spark erosion or a precision wheel cutter, and then abraded with a sufficiently fine SiC paper. Later, these specimens were solution treated in a dynamic vacuum at 1573 K for 5 h, → annealed in a static vacuum at 1373 K for 10 h → aged in a static vacuum at a temperature 1273 K for various times (ranging from 0 to 840 h), followed by a rapid cooling to room temperature, to obtain the dual two-phase microstructure.

Tensile tests were conducted in a temperature range between room temperature and 1173 K within a metal tube surrounded by an electron furnace, while those at temperatures beyond 1173 K were conducted within a vessel in which tungsten mesh heaters were assembled. Both types of furnace were evacuated to a vacuum degree of approximately 1.5×10^{-3}Pa before testing. The tensile specimens were deformed at a strain rate of 1.66×10^{-4}s^{-1}. The tensile elongation was calculated from the load-elongation curve drawn in the recorded chart and defined as plastic strain to fracture. The fracture surface of the tensile deformed specimens was examined by a scanning electron microscope (SEM).

Crystallography

The dual multiphase microstructure investigated in this study is composed of the Ni_3Al ($L1_2$) and Ni_3V ($D0_{22}$) phases that are fcc derivatives. Figure 3 shows the fcc, $L1_2$ and $D0_{22}$ structures and their ⟨100⟩diffraction patterns. The Ni_3Al with $L1_2$ structure has a lattice parameter of a = 0.3572 nm [16]. The Ni_3V with $D0_{22}$ structure is a tetragonal structure and has a lattice parameter of a = 0.3542 nm and c = 0.7212 nm [17], and transforms at T_c = 1318 K from a disordered fcc (A1) solid solution. The $L1_2$ ordering results in superlattice ⟨100⟩ and ⟨110⟩ reflections, while ordering to the $D0_{22}$ structure results in three rotational variants, with the c-axes along one of three ⟨100⟩ directions of the cubic lattice. Variant I (c//[010]) results in 1 1/2 0 superlattice reflections, variant II (c//[100]) results in 1/2 1 0 superlattice reflections, and variant III (c//[001]) results in 1 1 0 superlattice reflections. It is noted that in the following description the diffraction reflections are indexed in terms of the fcc (A1) structure in all diffraction patterns. Considering the small difference in lattice parameters of the phases, resulting in overlap of the reflections, it is difficult to detect the presence of either the $L1_2$ or fcc (A1) phase when all three $D0_{22}$ variants are present in a microstructure. However, different

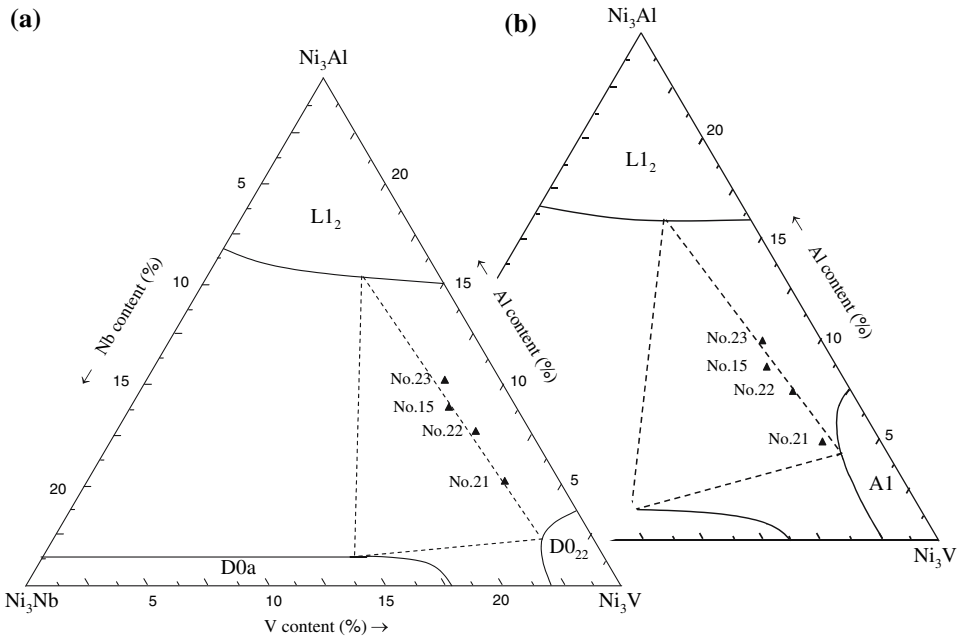

Fig. 1 Isothermal Ni_3Al–Ni_3Nb–Ni_3V pseudo-ternary phase diagrams at (**a**) 1273 K and (**b**) 1373 K [15]. Alloy compositions used in this study are plotted

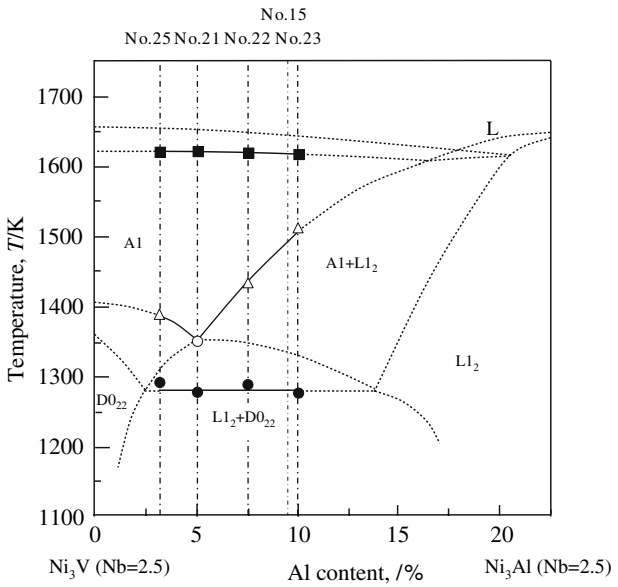

Fig. 2 Vertical section of the Ni_3Al–Ni_3Nb–Ni_3V pseudo-ternary phase diagram at 2.5 at.% Nb content

rotational variants of the $D0_{22}$ structure can be separately imaged by dark field using (I)1 1/2 0, (II)1/2 1 0 and (III)1 1 0 reflections.

Results

Microstructures

In order to obtain the dual two-phase microstructure, the alloys are primarily annealed at a temperature above the eutectoid temperature (1283 K), where the A1 and $L1_2$ phases are equilibrated, and then aged at a temperature below the eutectoid temperature. As a result, the two-phase microstructure has a hierarchy composed of the 'upper' two-phase ($L1_2 + A1$) microstructure (i.e., called the 'superalloy' microstructure) in the micron scale and the 'lower' two-phase ($L1_2 + D0_{22}$) microstructure in the sub-micron scale. Figure 4 shows a typical back-scattered electron image (BSE) of alloys No. 21, No. 22, No. 15 and No. 23 which were annealed at 1573 K for 5 h as a solution heat treatment, annealed at 1373 K for 10 h and then aged at 1273 K for 10 h, followed by a rapid cooling to room temperature. Alloy No. 21 with 5at.%Al exhibits almost a eutectoid microstructure (i.e., only the 'lower' two-phase microstructure) consisting of two-phase ($L1_2 + D0_{22}$). On the other hand, hyper eutectoid alloys No. 22, No. 15 and No. 23 exhibit the upper two-phase microstructure consisting of $L1_2$ phase precipitates and the fcc $(Ni)_{ss}$ matrix. It is noted that the volume fraction of $L1_2$ phase precipitates increases with Al content. Thus, the observed microstructures are consistent with the isothermal Ni_3Al-Ni_3Nb-Ni_3V pseudo-ternary phase diagram at 1373 K (Fig. 1) and the longitudinal phase diagram at 2.5 at.% Nb content shown in Fig. 2. Here, it is noted that boron doping by an amount of 0.05 wt.% does not affect the microstructure of the alloys.

The effect of aging time on the dual two-phase microstructure was investigated in detail in alloy No. 15 + B. Figure 5 shows the change of the *upper* multi-phase microstructure by aging time (from 5 h to 840 h) at 1273 K, although the *lower* multi-phase microstructure consisting of the ($L1_2 + D0_{22}$) phases is not resolved in this

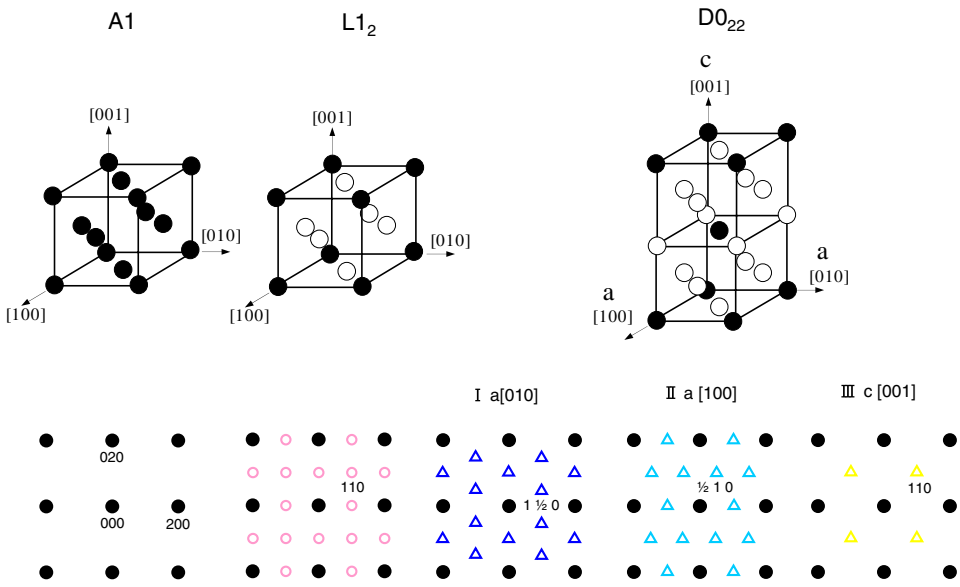

Fig. 3 Crystal structures and corresponding ⟨100⟩ zone axis diffraction patterns. Full and open marks represent fundamental and superlattice reflections, respectively. Note that the diffraction reflections are indexed in terms of fcc (A1) structure in all diffraction patterns

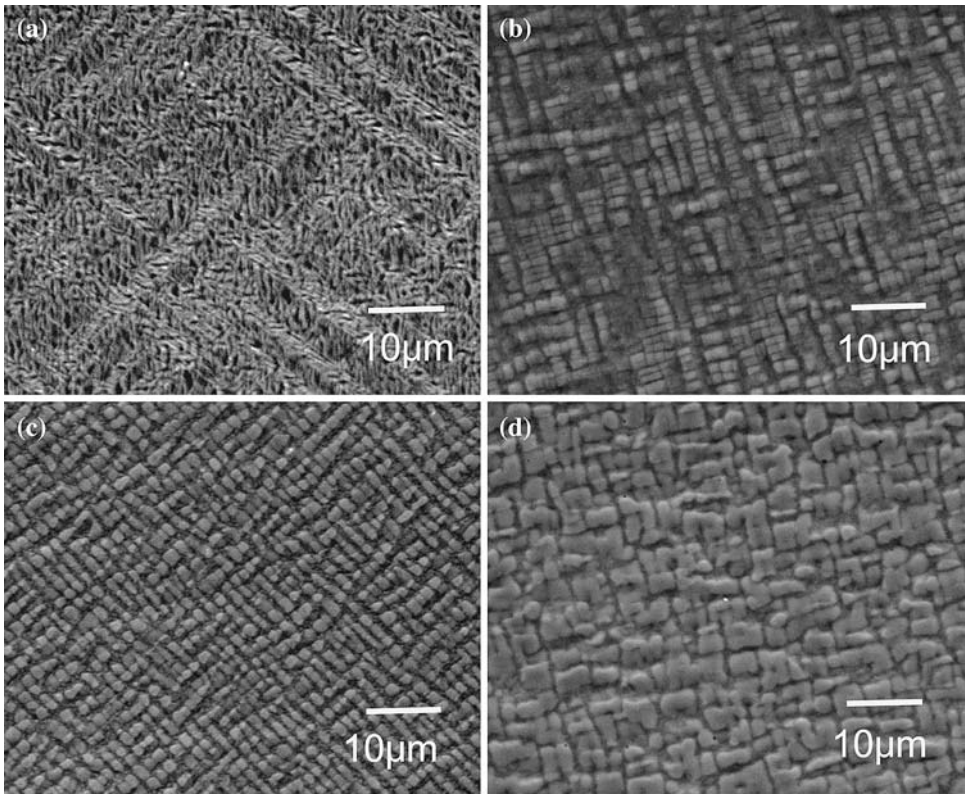

Fig. 4 Back-scattered electron image (BSE) of alloys (**a**) No. 21, (**b**) No. 22, (**c**) No. 15 and (**d**) No. 23, which were annealed at 1573 K for 5 h as a solution heat treatment, annealed at 1373 K for 10 h and then aged at 1273 K for 10 h, followed by a rapid cooling to room temperature. Note that the alloys were posted in order of Al content

SEM image. At an aging time of 5 h, the prior $L1_2$ phase precipitates are surrounded by the eutectoid region forming 'channel', whose microstructure is generally called 'superalloy' microstructure. That is, the cube planes {001} in the $L1_2$ phase tend to be parallel each other and become as the interfacial plane between the eutectoid region and the prior $L1_2$ phase precipitate. At aging time of 168 h, the cuboidal $L1_2$ phase precipitates somewhat degenerated although they still aligned along ⟨001⟩ directions. At a longest aging time of 840 h, the $L1_2$ phase precipitates changed from cuboidal to irregular shape and also tended to align along directions different from ⟨001⟩ directions. In addition, the habit (interfacial) planes between the prior $L1_2$ phase precipitate and the eutectoid region tended to change from {001} plane to different planes. However, the $L1_2$ phase precipitates did not so much coarsen in terms of

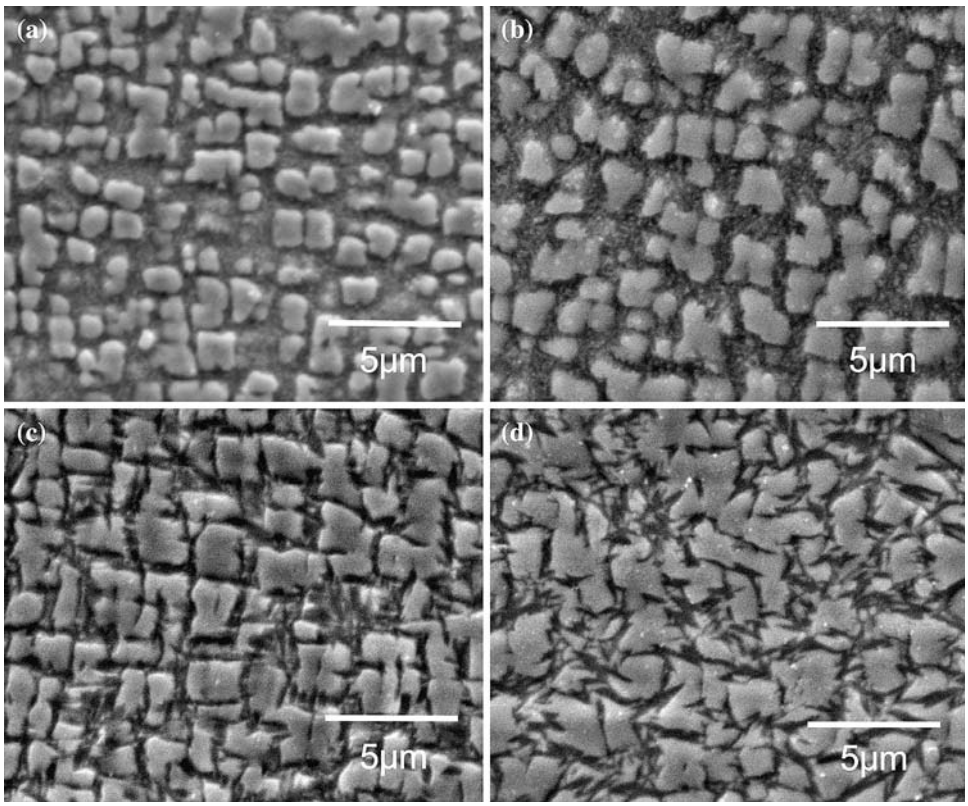

Fig. 5 Back-scattering (BS)-SEM images of the microstructure of the alloy No. 15 + B aged for (**a**) 5 h, (**b**) 10 h, (**c**) 168 h and (**d**) 840 h at 1273 K after annealing for 10 h at 1373 K

size and area fraction. Such a microstructural evolution for the upper two-phase microstructure is quite similar to that observed in the dual two-phase intermetallic alloys containing Ti [12].

In order to investigate the 'lower' two-phase microstructure, TEM analysis was performed on alloy No. 15 + B aged for 0 h, 10 h and 840 h at 1273 K after annealing for 10 h at 1373 K (Figs. 6–9). For the sample that was not aged (Fig. 6), phase decomposition already takes place in the lamellar-like form. The majority of lamellar-like structure aligns along two sets of orthogonal ⟨100⟩directions. Also, a selected area diffraction pattern (SADP) taken from the channel region shows the coexistence of superlattice reflections due to the $L1_2$ phase and the $D0_{22}$ variant structures I, II, and III, otherwise, superlattice diffractions only due to the $D0_{22}$ variant structures

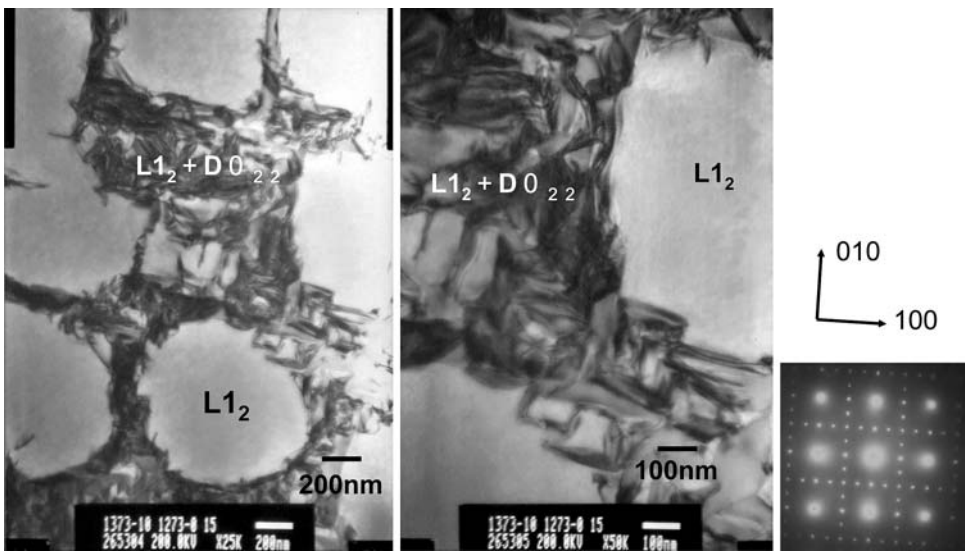

Fig. 6 TEM-bright-field images and selected area diffraction pattern (SADP) of alloy No. 15 + B aged for 0 h at 1273 K after annealing for 10 h at 1373 K. The SADP was taken from the eutectoid region, i.e., the 'channel-like form' area corresponding to the prior A1 phase

I, II, and III. In order to specifically identify the observed domains, dark-field images were taken using 1 1/2 0, 1/2 1 0, 1 1 0, and 1 0 0 reflections: the former three reflections result in the images corresponding to the $D0_{22}$ variant structures I, II, and III, respectively while the last reflection results in the image corresponding to the $L1_2$ phase. The analysis in Fig. 7 thus indicates that the eutectoid region contains the $L1_2$ phase and $D0_{22}$ phase with three variant structures I, II, and III.

For the sample aged for 10 h (Fig. 8), the bright field image in the eutectoid region shows that the morphology is similar to that observed in the sample without aging. However, the size (i.e., spacing) of the lamellar-like structure becomes larger and the contrast becomes more intensive, indicating that the phase separation certainly proceeds. In this aging time, the corresponding SADP shows the coexistence of superlattice diffractions of the $L1_2$ phase and $D0_{22}$ phase with three variant structures I, II, and III. Also, it is observed that the majority of lamellar-like structure aligns along the two sets of orthogonal ⟨100⟩ directions.

For the sample aged for a prolonged time (840 h) (Fig. 9), it is evident that the lamellar-like structure much coarsened but the morphology (regarding the direction and interfacial plane of the lamellar structure) is similar to those of the specimens aged for shorter time. As understood from SADP, one interesting result at this aging time is that the diffraction spots corresponding to the $L1_2$ phase becomes weak. This result reveals that the volume fraction of the $L1_2$ phase in the lamellar-like structure becomes

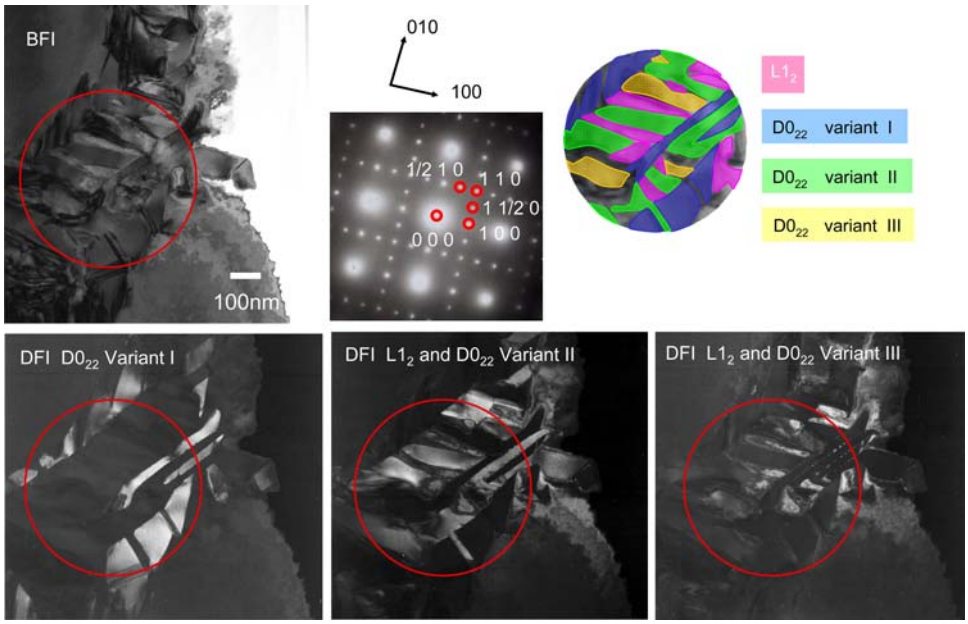

Fig. 7 Bright- and dark- field images, and SADP of the microstructure of alloy No. 15 + B aged for 0 h at 1273 K after annealing for 10 h at 1373 K. Areas corresponding to the $L1_2$ phase and the $D0_{22}$ variant structures I (or II) and III are schematically shown in the right-top corner

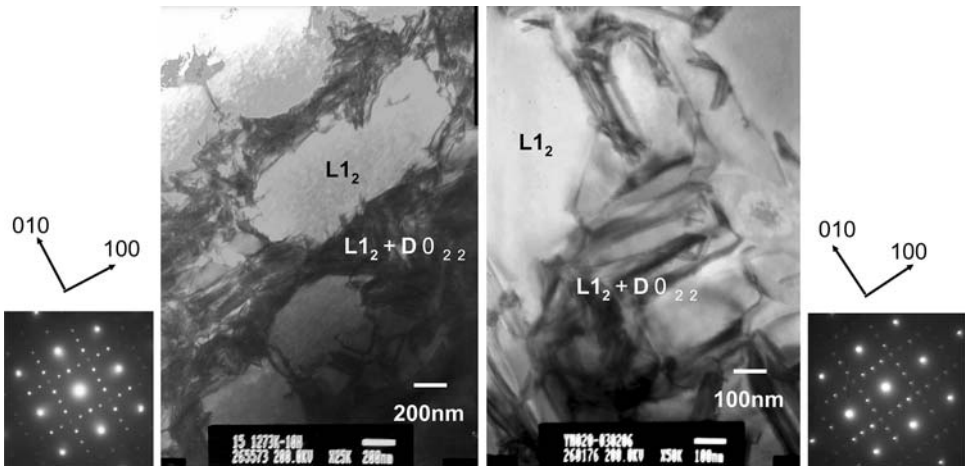

Fig. 8 TEM-bright- field images and selected area diffraction patterns (SADPs) of alloy No. 15 + B aged for 10 h at 1273 K after annealing for 10 h at 1373 K. The SADP was taken from the eutectoid microstructure, i.e., the 'channel-like form' area corresponding to the prior A1 phase

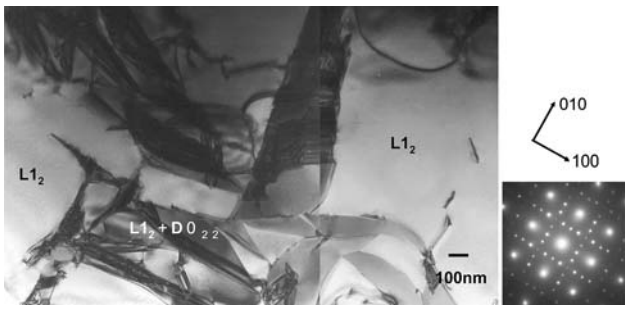

Fig. 9 TEM-bright- field image and selected area diffraction pattern (SADP) of alloy No. 15 + B aged for 840 h at 1273 K after annealing for 10 h at 1373 K The SADP was taken from the eutectoid microstructure, i.e., the 'channel-like form' area corresponding to the prior A1 phase. The beam direction used in these conditions is $[001]_{L12}$

smaller than that observed in the samples aged at shorter times. Quite similar results were observed in different eutectoid areas.

Mechanical properties

Using the samples aged at 1273 K for various times (ranging from 0 to 840 h) after annealing for 10 h at 1373 K, tensile tests were performed as a function of temperature. As an example, Fig. 10 shows yield strength, tensile strength and tensile elongation as a function of temperature for alloys No. 15 + B and No. 22 + B that were aged at 1273 K for 10 h after annealing for 10 h at 1373 K, respectively. In both alloys, the yield strength as well as the tensile strength increased with increasing temperature, and showed a broad maximum at intermediate temperature (around 900 K), followed by a decrease at high temperature. Accordingly, positive temperature dependence of the flow strength took place, and at a peak temperature (900 K), the tensile strength, as well as the yield strength exceeded 1GPa.

At low temperature, boron-doped alloys (i.e., No. 15 + B and No. 22 + B) showed a relatively large strain-hardening rate after yielding and then ruptured. With increasing temperature, the strain-hardening rate decreased. At a peak temperature, the strain-hardening rate after yielding was still positive. At high temperature (beyond 873 K), alloys exhibited steady-state flow after yielding and subsequent yield drop, and then ruptured after strength decrease. The tensile elongation ranged between 0.4 and 3% at room temperature, and remained up to 1273 K, as shown in Fig. 10.

Figure 11 shows variation of room temperature Vickers hardness with aging time for alloys No. 15 + B and No. 22 + B that were aged at 1273 K. The hardness level was higher in alloy 22 + B than in alloy 15 + B through a whole aging time, reflecting that the former alloy contained a larger volume fraction of the eutectoid microstructure than the latter alloy. The previous study showed that the flow strength basically depended on the ratio of the volume fraction of the large $L1_2$ precipitates to the eutectoid region, that is, the hardness or the strength decreases with increasing this ratio [15]. In both alloys, the Vickers hardness was primarily insensitive to aging time up to about 10^5 s ($\sim$28 h), and then gradually decreased in the time range beyond 10^5 s, probably owing to the coarsening of the microstructure.

Figure 12 shows variations of tensile strength and tensile elongation with aging time for alloys No. 15 + B (a) and No. 22 + B (b) that were aged at 1273 K, respectively. Deformation was carried out at room temperature, 873 and 1073 K. In both alloys, it appears that the tensile strengths were primarily insensitive to aging time up to 10^6 s

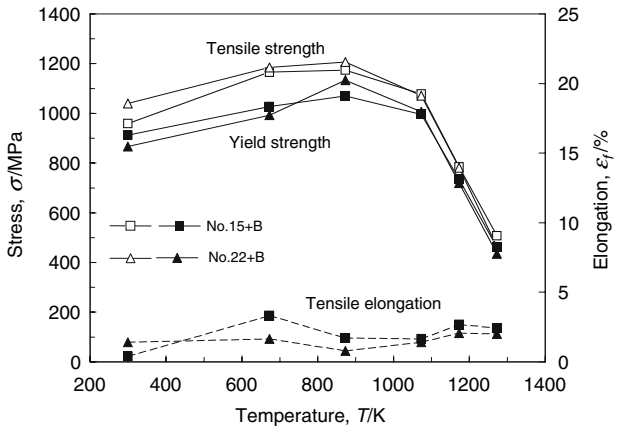

Fig. 10 Tensile strength, yield strength and tensile elongation as a function of test temperature for the alloys No. 15 + B and No. 22 + B with the dual two-phase microstructure

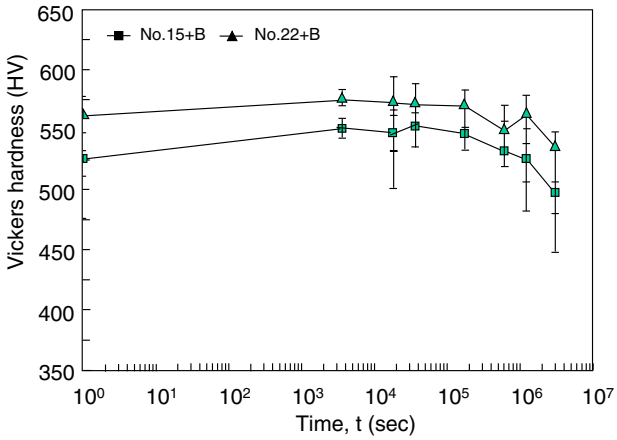

Fig. 11 Variation of room-temperature Vickers hardness with aging time for alloys No. 15 + B and No. 22 + B that were aged at 1273 K

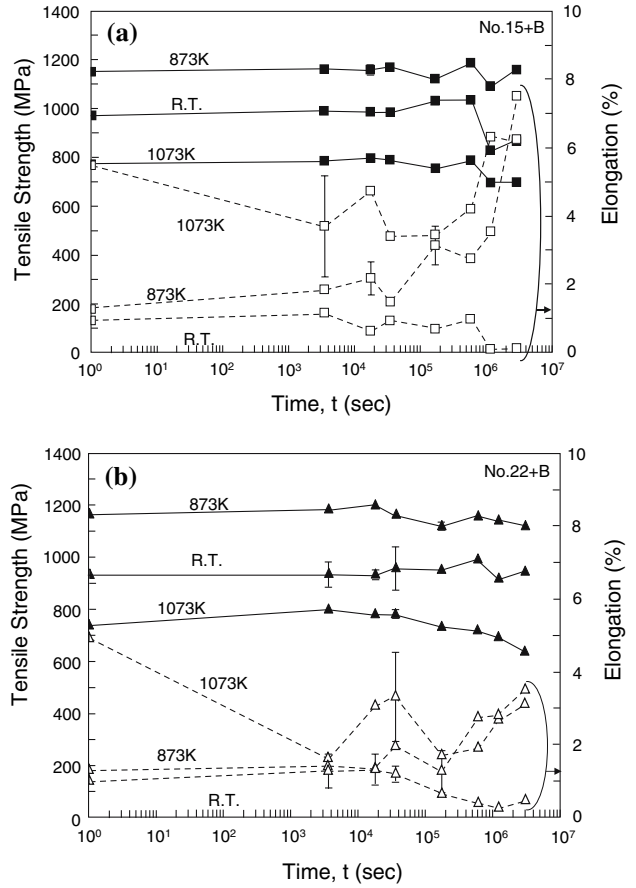

Fig. 12 Variation of tensile strength and tensile elongation with aging time for alloys (**a**) No. 15 + B and (**b**) No. 22 + B that were aged at 1273 K, and then deformed at room temperature, 873 K and 1073 K

(∼278 h), but tended to decrease in aging time range beyond 10^6 s (∼278 h), especially for the samples deformed at high temperature. On the other hand, the tensile elongations were similarly insensitive to aging time up to 10^6 s (∼278 h) although data were largely scattered. At aging time range beyond 10^6 s (∼278 h), the tensile elongation of the samples deformed at room temperature decreased while the tensile elongation of the samples deformed at intermediate (873 K) and high (1073 K) temperatures steadily increased. It appears that the changes of two mechanical properties at aging time range exceeding10^6 s (∼278 h) are due to the coarsening of the dual two-phase microstructure.

In boron-free alloys, preferential fracture path was grain boundaries. However, the fracture mode changed from intergranular fracture to transgranular fracture by boron doping. Figure 13 shows SEM fractography as a function of aging time for the alloy No. 15 + B that was aged at 1273 K and then deformed at room temperature. The observed fracture patterns reveal transgranular fracture mode accompanied with dimple-like and cleavage-like patterns, but tend to be more or less facetted on a certain crystallographic plane, reflecting the specific microstructure of the present alloy, i.e., the dual two-phase microstructure. For the sample without aging, the cleavage-like patterns were prevailing while for the samples aged for longer time the dimple-like fracture patterns were prevailing. Figure 14 shows SEM fractography, as a function of aging time for the alloy No. 15 + B that was aged at 1273 K and then deformed at high temperature, 1073 K. The observed fracture patterns reveal transgranular fracture mode accompanied with more dimple-like patterns than those observed in the samples deformed at room temperature. The cleavage-like fracture patterns were not observed in the samples deformed at high temperature. Thus, the fracture patterns observed at both temperatures indicate that energy-dissipated event occurs during propagation of micro crack, resulting in a certain level of tensile ductility irrespective of aging time.

Discussion

The feature of the microstructure and its evolution observed in the present dual two-phase intermetallic alloys is basically similar to those observed in the dual two-phase intermetallic alloys containing Ti [12]. The prior A1 phase undergoes eutectoid reaction at a lower temperature than a eutectoid temperature (∼1283 K) and decomposes into the $L1_2$ and $D0_{22}$ phases in the lamellar-like form along cube directions and on cube planes. The $D0_{22}$ phase involves domains with two or three different structural variants. As annealing time proceeds, the decomposed two phases steadily increase and the $L1_2$ phase appears to be eliminated from the constituent phases in the lamellar-like microstructure (Fig. 9). However, the results different from those observed in the previous study [12] are also pointed out: in the dual two-phase intermetallic alloys containing Ti [12] the direction and interfacial plane of the lamellar rotates (i.e., changes) from ⟨001⟩ to ⟨001⟩ and {001} to {011}, respectively while in the present dual two-phase intermetallic alloys the direction and interfacial plane of the lamellar remain ⟨001⟩ direction and {001} plane, respectively even at a prolonged aging time (e.g., 840 h). From the diffusional point of view, the addition of Nb with a higher melting point than Ti is assumed to have the effect of retarding the microstructural evolution, therefore consistent with the present result. However, this discrepancy may be also associated with the difference in alloying element, Ti and Nb through affecting the free energy change for the microstructure and its evolution that is comprised by the chemical free energy term, the interfacial energy term and the elastic strain energy term [18–21].

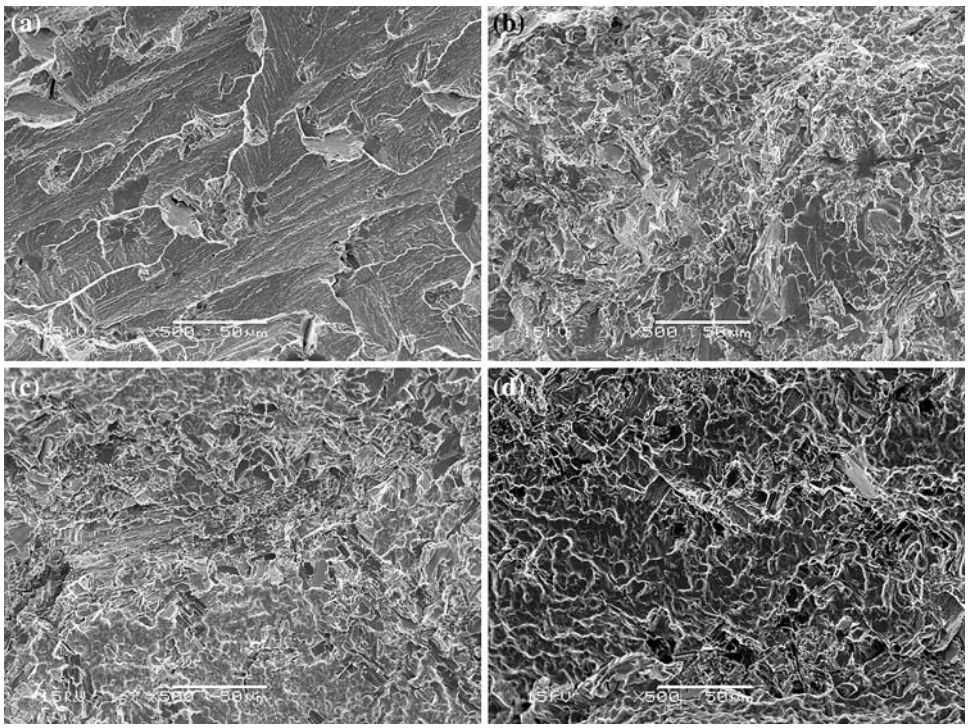

Fig. 13 Variation of fracture pattern with aging time for alloy No. 15 + B that was aged at 1273 K for (**a**) 0 h, (**b**) 10 h, (**c**) 168 h and (**d**) 840 h, and then deformed at room temperature

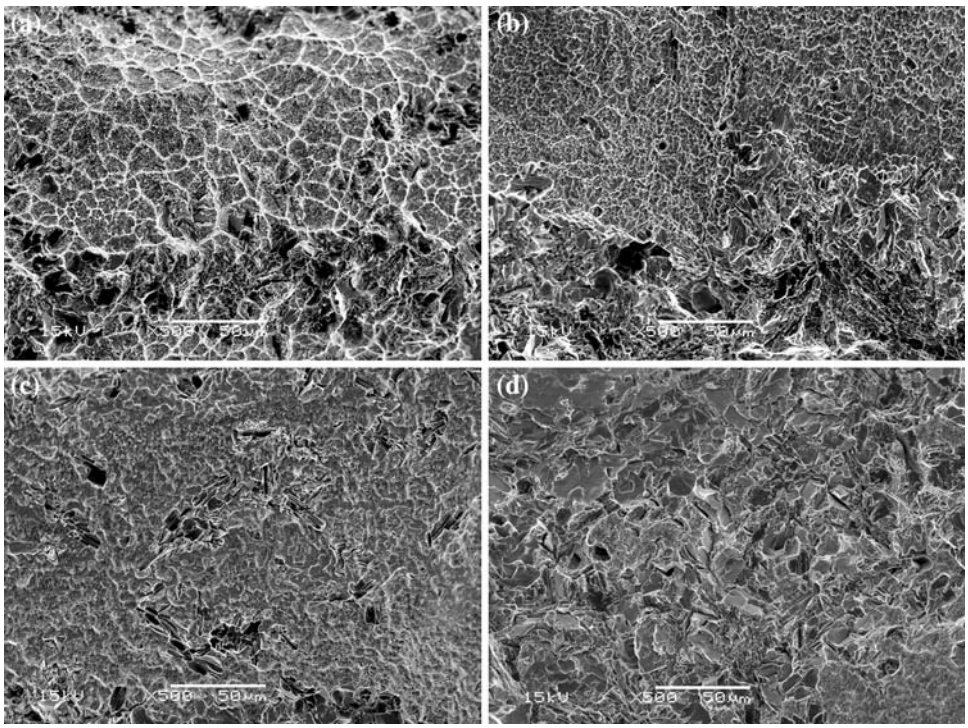

Fig. 14 Variation of fracture pattern with aging time for alloy No. 15 + B that was aged at 1273 K for (**a**) 0 h, (**b**) 10 h, (**c**) 168 h and (**d**) 840 h, and then deformed at 1073 K

Actually, the feature of the microstructure and its evolution observed in binary Ni_3V alloys [22–25] and also those observed in near eutectoid Ni_3Al-Ni_3V pseudo-binary alloys [26, 27] has been argued based on such a chemical free energy term. However a decisive explanation is not given at the present time.

The yield strength anomaly shown in Fig. 10 primarily arises from the fact that the GCP Ni_3X phases, Ni_3Al ($L1_2$) and Ni_3V ($D0_{22}$) display the positive temperature dependence of the flow (or yield) stress [28–31]. In these GCP Ni_3X phases, the anisotropy in the anti-phase boundary (APB) energy between the glide plane and non-glide plane

promotes thermally activated cross-slip of the dissociated screw dislocation from the glide plane to non-glide plane, resulting in the strength anomaly. Besides the strength anomaly, large interfacial strengthening occurs in the present dual two-phase intermetallic alloys when a dislocation passes through the interface between the $L1_2$ and $D0_{22}$ phases or between different variants in the $D0_{22}$ phases.

Over a wide range of temperatures, a certain amount of tensile ductility was observed in the present dual two-phase intermetallic alloys. As one of corresponding explanations, two constituent phases, Ni_3Al ($L1_2$) and Ni_3V ($D0_{22}$) have relatively simple structures, and therefore are plastically deformable in a wide temperature range. Also, the deformation of Ni_3Al ($L1_2$) satisfies the von Mises criterion for the general plasticity of polycrystalline material, activating $1/2\langle 110\rangle\{111\}$ slip systems [32]. Furthermore, it has been reported that Ni_3V ($D0_{22}$) can be deformed by activating $\langle 112\rangle\{111\}$ slip system in a wide temperature range [33]. Second, the present dual two-phase intermetallic alloys are composed of fine microstructures and have certain orientation relationships between the constituent phases with highly coherent interfacial structures. The number of dislocation piled-up against the interface is reduced in such a microstructure, and consequently the initiation and subsequent propagation of the micro cracks are suppressed.

Last, it is demonstrated that the effect of the microstructural evolution on the mechanical properties of the present dual two-phase intermetallic alloys is primarily not so much significant at least up to the aging time of 10^6 s ($\sim$278 h) at 1273 K, and small even in the aging time range exceeding 10^6 s ($\sim$278 h). As one of the merits expected from this result, to obtain an optimum microstructure resulting in excellent high-temperature mechanical property, a relatively broad range of heat treatment scheme is permitted. Also, it is anticipated from this result that the microstructural stability under loading at high temperature is high and consequently creep strength is expected to be excellent. In fact, high creep strength has been observed in the dual two-phase intermetallic alloys containing Ti [13] and Nb [15].

Conclusions

Dual two-phase intermetallic alloys composed of geometrically close packed (GCP) structures of Ni_3Al ($L1_2$) and Ni_3V ($D0_{22}$) containing Nb were investigated to clarify the microstructural evolution during low-temperature annealing (aging) and the related mechanical properties. The following results were obtained from the present study.

(1) The eutectoid region, i.e., the prior Al phase (Ni solid solution) was composed of the lamellar-like structure consisting of Ni_3Al ($L1_2$) and Ni_3V ($D0_{22}$) even at early aging stage, and then coarsened with increasing aging time.
(2) The lamellar-like structure aligned along $\langle 001\rangle$ direction and on $\{001\}$ plane in the prior A1 phase (or the $L1_2$ phase). Also, the Ni_3V ($D0_{22}$) phase had three different variant structures.
(3) It was found that in a wide range of temperature, the dual two-phase intermetallic alloys showed high yield and tensile strength, and also reasonable tensile ductility, accompanied with ductile fracture mode.
(4) The observed mechanical properties were less sensitive to the microstructural evolution during low-temperature annealing (aging), meaning that the present dual two-phase intermetallic alloys are expected to be excellent for creep property and, therefore, promising for a new type of high-temperature structural material.

Acknowledgement This work was supported in part by the Grant-in-aid for Scientific Research (B) from the Ministry of Education, Culture, Sports and Technology. Also, a part of this work was carried out under the Visiting Researcher's Program of Advanced Research Center of Metallic Glasses, Institute for Materials Research, Tohoku University.

References

1. Van Vucht JHJ (1966) Less-Common Met 11:308
2. Sinha AK (1969) Trans Met Soc AIME 245:911
3. Sinha AK (1972) Prog In Mater Sci Part 2 15:79
4. Tomihisa K, Kaneno Y, Takasugi T (2002) Intermetallics 10:247
5. Ohira K, Kaneno Y, Takasugi T (2004) J Mater Sci 39:2295
6. Tomihisa K, Kaneno Y, Takasugi T (2004) Intermetallics 12:317
7. Ohira K, Kaneno Y, Takasugi T (2005) Mat Sci Eng A 399:332
8. Fujita M, Kaneno Y, Takasugi T. Mat Sci Eng A (in press)
9. Nunomura Y, Kaneno Y, Tsuda H, Takasugi T (2004) Intermetallics 12:389
10. Nunomura Y, Kaneno Y, Tsuda H, Takasugi T (2006) Acta Mater 54:851
11. Shibuya S, Kaneno Y, Yoshida M, Takasugi T (2006) Acta Mater 54:861
12. Shibuya S, Kaneno Y, Tsuda H, Takasugi T (2007) Intermetallics 15:338
13. Shibuya S, Kaneno Y, Yoshida M, Shishido T, Takasugi T (2007) Intermetallics 15:119
14. Soga W, Kaneno Y, Takasugi T (2006) Intermetallics 14:170
15. Soga W, Kaneno Y, Yoshida M, Takasugi T (2007) Mat Sci Eng A (in press)
16. Pearson WB (1958) A handbook of lattice spacing and structures of metals and alloys, Pergamon press, p 378
17. Villars P, Calvert LD (1986) Pearson's handbook of crystallography data for intermetallic phases, vol. 3. ASM, Metals Park, p 2907
18. Suzuki T, Mishima Y, Miura S (1989) ISIJ Int 29:1
19. Hagihara K, Nakano T, Umakoshi Y (2000) Acta Materialia 48:1469

20. Hagihara K, Nakano T, Umakoshi Y (2003) Scripta Mater 48:577
21. Hagihara K, Nakano T, Umakoshi Y (2003) Acta Mater 51:2623
22. Tanner LE (1968) Phys Stat Sol 30:685
23. Sihgh JB, Sundararaman M, Mukhopadhyay P, Prabhu N (2003) Scripta Mater 48:261
24. Sihgh JB, Sundararaman M, Mukhopadhyay P , Prabhu N (2003) Intermetallics 11:83
25. Suzuki A, Kojima H, Matsuo T, Takeyama M (2004) Intermetallics 12:969
26. Bendersky LA, Biancaniello FS, Williams ME (1994) J Mater Res 9:3068
27. Takeyama M, Kikuchi M (1998) Intermetallics 6:573
28. Pope DP, Ezz SS (1984) Int Mater Rev 29:136
29. Stoloff NS (1989) Int Mater Rev 34:153
30. Yamaguchi M, Umakoshi Y (1990) Prog Mater Sci 34:1
31. Hagihara K, Tanaka T, Nakano T, Umakoshi Y (2005) Acta Mater 53:5051
32. von Mises R (1928) Z Ang Math Mech 8:161
33. Hagihara K, Mori M, Umakoshi Y (2007) MRS Proc Publ 980:II05-20